



# 1      **Sea-surface temperature variability and climate drivers in** 2      **Cuba's Jardines de la Reina National Park (2003–2022)**

3

4      Maibelin Castillo-Alvarez<sup>1,2</sup>; Oscar Pizarro<sup>2,3</sup>; Alain Muñoz-Caravaca<sup>4</sup>; Iván Pérez-Santos<sup>5,6</sup>;  
5      David Carrasco<sup>2</sup>; David Francisco Bustos-Usta<sup>1,6</sup>; Laura Castellanos-Torres<sup>1,2,4</sup>

6

7      <sup>1</sup> Postgraduate Program in Oceanography, Department of Oceanography, Faculty of Natural Sciences and  
8      Oceanography. Universidad de Concepción, Chile.

9      <sup>2</sup> Millennium Institute of Oceanography (IMO), Universidad de Concepción, Chile.

10      <sup>3</sup> Department of Geophysics, Universidad de Concepción, Chile.

11      <sup>4</sup> Centro de Estudios Ambientales de Cienfuegos. AP 5, 59350, Ciudad Nuclear, Cienfuegos, Cuba.

12      <sup>5</sup> Centro i-mar, Universidad de los Lagos, Puerto Montt 5480000, Chile

13      <sup>6</sup> Center for Oceanographic Research COPAS Sur-Austral and COPAS COASTAL (FB210021), Universidad  
14      de Concepción, Chile.

15

16

17      Correspondence to: [mcastilloa@udec.cl](mailto:mcastilloa@udec.cl) and [opizarro@udec.cl](mailto:opizarro@udec.cl)

18

19      **Abstract.** Coral reef systems on the southeastern Cuban shelf are exposed to rapid warming and increasingly  
20      frequent marine heatwaves (MHWs). However, the physical drivers of local sea-surface temperature (SST)  
21      variability remain poorly quantified. The present study examines seasonal-to-decadal SST variability in and  
22      around the Jardines de la Reina National Park (JRNP) and investigates the extent to which atmospheric–ocean  
23      processes and large-scale climate modes influence that variability. The study analyses daily 1-km Multi-Scale  
24      Ultra High Resolution (MUR) SST from 2003–2022, in conjunction with ERA5 surface heat fluxes and  
25      GLORYS12 mixed-layer fields. A mixed-layer heat budget, compiled from daily values and averaged to  
26      monthly values, is used to attribute the seasonal cycle; long-term trends, MHWs and modes of variability  
27      (Orthogonal Functions) can be used to explain interannual to decadal changes and their links to El Niño  
28      Southern Oscillation (ENSO), the Western Hemisphere Warm Pool (WHWP), the Tropical North Atlantic  
29      (TNA) and the North Atlantic Oscillation (NAO).

30      Net air–sea heat exchange sets the seasonal evolution of SST, whereby horizontal advection provides a smaller  
31      modulation near the shelf break; a characteristic ~2-month lead of heat flux over temperature is consistent with  
32      mixed-layer heat storage. This thermodynamic control explains a marked autumn–winter shelf–offshore  
33      contrast between the shallow gulfs (Gulfs of Ana María and Guacanayabo) and the adjacent Caribbean Sea.  
34      Superimposed over this area is a warming trend of ~0.28°C decade<sup>-1</sup> (strongest in winter/transition months,  
35      peaking around April at ~0.48°C and November at ~0.35°C decade<sup>-1</sup>) and a step-like shift in 2011–2013 towards  
36      a persistently warmer state. MHWs intensified during the second decade; the mean event-wise maximum  
37      intensity was higher inside GAM, while upper categories occurred more frequently offshore. EOF1 (87.5%) is  
38      a basin-wide mode linked on an interannual basis to ENSO/WHWP and latent-heat flux and at low frequency  
39      to the NAO, while EOF2 (6.2%) captures a shelf–offshore dipole related to TNA.



40 The aforementioned results provide a physical basis for which to issue early warnings from forecasts of net heat  
41 flux and mixed-layer depth, thus encouraging the use of regional high-resolution modeling and targeted  
42 observations. Key limitations to the present study include a 20-year MHW baseline and an under-resolution of  
43 currents in highly shallow and complex bathymetry.

## 44 1. Introduction

45 Sea surface temperature (SST) is a key regulator of marine ecosystems, since it drives physical, chemical and  
46 biological processes. Its variability has profound implications for coastal and oceanic regions in a warming  
47 climate (Venegas et al., 2023). Since the industrial era, anthropogenic pressures have altered ocean dynamics  
48 and accelerated habitat degradation (Jackson et al., 2014; Lotze et al., 2006). Rising SSTs are closely linked to  
49 coral bleaching, habitat fragmentation and biodiversity loss in tropical regions (Bruno et al., 2019; Hughes et  
50 al., 2003). Coral reef ecosystems are susceptible to temperature fluctuations and to co-occurring stressors,  
51 including light, sedimentation and chemical changes (Cramer et al., 2020). As a result, understanding the  
52 patterns and drivers of SST variability has become crucial in order to predict ecological impacts and inform  
53 conservation efforts.

54 The Caribbean Sea (CS) hosts extensive coral reefs and numerous marine protected areas (MPAs), which are  
55 central to regional conservation and livelihoods. The Jardines de la Reina National Park (JRNP), the largest  
56 marine reserve in Cuba and one of the largest in the Caribbean, is notable due to its exceptional reef conditions  
57 and biodiversity (Appeldoorn and Lindeman, 2003; Linton et al., 2002; Gerhartz-Muro et al., 2018). Yet, JRNP  
58 faces a number of challenges typical of Caribbean reefs, including the dramatic decline of historically dominant  
59 species, such as *Acropora palmata*, now classified as critically endangered (Caballero-Aragón et al., 2020).  
60 Prior work at JRNP has focused primarily on reef ecology and conservation status (Hernández-Fernández et al.,  
61 2011, 2016, 2019a; Pina Amargós et al., 2011), with fewer studies addressing the physical drivers that modulate  
62 local thermal stress and ecosystem vulnerability. This research gap is significant, since thermal extremes and  
63 the persistence thereof increasingly govern the risk of coral bleaching across the region (van Hooidek et al.,  
64 2015; Graham et al., 2015; Mumby et al., 2014).

65 At a broader scale, southern Cuba exhibits warmer SST than the northern shelf of the island, influenced by  
66 exchanges with the CS (Cerdeira-Estrada et al., 2005; Chollett et al., 2012; Caravaca et al., 2022; González-De  
67 Zayas et al., 2022). Basin-wide analyses also point to a significant warming trend during recent decades, which  
68 are particularly pronounced to the south of Cuba (Avila-Alonso et al., 2020). However, existing studies provide  
69 merely a partial view of SST variability on the southeastern Cuban shelf and seldom disentangle the relative  
70 roles of air-sea heat fluxes, horizontal advection and large-scale climate modes in shaping local conditions  
71 within and adjacent to JRNP.

72 Large-scale atmospheric variability modulates Caribbean SST through several well-documented pathways. The  
73 El Niño Southern Oscillation (ENSO) influences trade winds and latent heat flux over the Western Hemisphere  
74 Warm Pool (WHWP), defined as the region warmer than 28.5°C in the Western Tropical Atlantic and in the



75 eastern North Pacific, which alter regional SST at interannual scales (Wang and Enfield, 2001, 2003; Czaja et  
76 al., 2002). The North Atlantic Oscillation (NAO) affects wind patterns, precipitation and heat exchange across  
77 the North Atlantic–Caribbean system, including via the Caribbean Low-Level Jet (Hurrell, 1995; Wang et al.,  
78 2007; Cook & Vizzy, 2010). Additional variability arises from the Tropical North Atlantic (TNA) and WHWP  
79 indices, which capture shifts in regional SST (Enfield et al., 1999; Enfield and Lee, 2005). The process of  
80 clarifying how these climate modes project onto local SST in the shelf versus adjacent oceanic waters near  
81 JRNP is crucial for efforts to link physical forcing with ecological risk.

82 In the present study, the authors investigate seasonal-to-decadal variability of sea-surface temperature in and  
83 around JRNP and its controlling mechanisms using daily 1-km Multi-Scale Ultra High Resolution (MUR) SST  
84 (2003–2022), ERA5 dataset surface heat fluxes, and GLORYS12 (1/12°) dataset currents/temperature by: (i)  
85 resolving the seasonal cycle and diagnosing the mixed-layer heat budget to gauge air–sea heat exchange versus  
86 horizontal advection; (ii) quantifying long-term trends and testing for regime shifts; (iii) detecting and  
87 characterizing marine heatwaves (MHWs); and (iv) extracting dominant modes via Empirical Orthogonal  
88 Functions (EOFs) and relating them to the El Niño–Southern Oscillation, the North Atlantic Oscillation, the  
89 Tropical North Atlantic, and the Western Hemisphere Warm Pool.

90 Accordingly, the authors of the present research address three working hypotheses: (1) at seasonal scales, air–  
91 sea heat fluxes dominate SST variability, with shallow shelf waters exhibiting stronger amplitude and faster  
92 cooling/warming than adjacent oceanic waters; (2) interannual variability shows modulation by ENSO/WHWP  
93 and TNA via latent-heat-flux anomalies and circulation changes; and (3) decadal changes in the region,  
94 including post-2010 regime shifts, are consistent with NAO-related variations in atmospheric forcing. By  
95 resolving shelf–offshore contrasts and attributing variability across time scales, the analysis herein provides a  
96 physical basis for interpreting recent and future thermal stress in this MPA in addition to anticipating ecosystem  
97 responses under continued warming.

## 98 **2. Data and methods**

### 99 **2.1 Study region: Jardines de la Reina National Park (JRNP)**

100 The JRNP lies on the southeastern Cuban shelf, bordered to the north by the Gulf of Ana María (GAM), to the  
101 east by the Gulf of Guacanayabo (GG) and to the south by the CS (Figure 1). The archipelago comprises ~661  
102 cays (keys) that extend east–west and which are fringed by mangroves. According to Pina Amargós et al.  
103 (2011), the protected area covers 217,036 ha, of which 200,957 ha are marine hectares. The seafloor shows a  
104 marked north–south contrast: to the north, the shallow GAM is characterized by extensive flat banks, seagrass  
105 beds and soft sediment with a general depth of < 20 m; to the south, the shelf edge transitions abruptly to a steep  
106 continental slope descending to > 3,000 m. This sharp gradient underpins a mosaic of habitats, from shallow  
107 coastal ecosystems to deep-sea environments.

108 The region has a tropical climate with two boreal seasons: a wet season (May–October) and a dry season  
109 (November–April). Prevailing trade winds are generally northeasterly and strengthen during the dry season



(Pérez-Santos et al., 2010). Sea-level pressure follows a seasonal cycle, with higher values in boreal winter (January–March) under the influence of the subtropical high, and lower values in summer (July–September) as the intertropical convergence zone approaches (Waliser and Jiang, 2015). Air temperatures are warm year-round (~24–30°C) and there is modest interannual variability, despite pronounced diurnal and seasonal cycles. Summer is warmest while winter is slightly cooler (Caravaca et al., 2022). On the southeastern Cuban shelf, the mean flow is westward under the prevailing easterlies (Emilsson and Tápanes, 1971). It is modulated by tides and currents from the adjacent ocean, notably the Caribbean Current (Arriaza et al., 2008). Tides are mixed and microtidal, and exert little direct control on the mean shelf circulation, although tidal currents can enhance vertical mixing (Emilsson and Tápanes, 1971; Arriaza et al., 2008).

## 2.2 SST data

Sea-surface temperature was obtained from the Group for High Resolution Sea Surface Temperature MUR Level-4 analysis produced by the NASA Jet Propulsion Laboratory. This product provides daily global fields at ~1 km (0.01°) by blending multiple infrared and microwave satellite sensors (Chin et al., 2017) and is widely used in tropical reef and coastal studies (for example, Kumagai and Yamano, 2018; Skerrett et al., 2024). The present study analyzed data from 2003 to 2022 and subsequently subset the domain, as shown in Figure 1.

All processing was performed on the native 1km grid, unless otherwise specified. Daily fields were: (i) land-masked and quality-screened using the product masks; (ii) averaged to monthly means for the long-term, seasonal and EOF analyses; and (iii) converted to monthly anomalies by removing the 2003–2022 monthly climatology (further details are provided in Section 2.5). For diagnostics requiring co-location with reanalyses (mixed-layer heat budget and horizontal advection), SST was bilinearly remapped to the target grid (GLORYS12 at 1/12° or ERA5 at 1/4°) to avoid artificial gradients from mismatched resolutions. All temperatures are reported in °C.

The authors of the present research retained the 1-km fields to depict frontal structures in Figure 2; frontal overlays are computed from local SST differences (threshold  $\geq 0.5^\circ\text{C}$ ) and lightly smoothed with a 3×3 neighbourhood operator to suppress pixel-scale noise.

It should be noted that MUR SST was not used in the mixed-layer heat budget (Section 2.6); there, authors diagnosed temperature tendencies ( $\partial T/\partial t$ ) using the GLORYS12 mixed-layer temperature (MLT), depth and currents for reasons of internal consistency with regards to the terms. At monthly scales, MUR SST and GLORYS12 MLT were correlated throughout the study area, thus, variability in MLT is interpreted as the explanation for the observed SST variability.

## 2.3 Atmospheric fluxes (ERA5) and ocean reanalysis (GLORYS12)

The present study used ERA5 surface flux components (shortwave, longwave, latent and sensible) and 10 m winds at native hourly resolution, aggregated to daily and then monthly means for the period 2003–2022. The upper-ocean state was characterized with GLORYS12 at daily resolution (temperature, horizontal currents and



144 Ocean Mixed Layer Thickness), with monthly means used for non-budget diagnostics. Heat flux was measured  
145 in  $\text{W m}^{-2}$ . The oceanographic convention that holds that positive net heat flux warms the ocean was adopted  
146 throughout the course of the present research.

147 The upper-ocean state was characterized by GLORYS12 (eddy-resolving,  $1/12^\circ$ , 50 vertical levels, daily), from  
148 which potential temperature, horizontal currents and mixed layer depth and temperature were extracted over  
149 the same period. Fields were subset to the domain shown in Figure 1 and, where necessary, bilinearly remapped  
150 to a standard grid (ERA5-GLORYS12) for the mixed-layer heat budget and advection diagnostics. Regarding  
151 the budget, ERA5 fluxes were first aggregated to daily values and then bilinearly remapped to the GLORYS12  
152 grid; the results were subsequently averaged to a monthly basis. For descriptive analyses, monthly fields were  
153 utilized.

## 154 2.4 Climate indices

155 The present study used a monthly time series of large-scale climate indices known to modulate Caribbean SST.  
156 The ENSO was represented by the Multivariate ENSO Index v2 (MEI.v2) (Zhang et al., 2019; Wolter, 1993),  
157 obtained from the NOAA Physical Sciences Laboratory (PSL). The WHWP index (Wang and Enfield, 2001,  
158 2003; Enfield and Lee, 2005; Wang et al., 2006) and the TNA index (Enfield et al., 1999; Chen et al., 2021)  
159 were also taken from NOAA PSL. The NAO index was obtained from the NOAA Climate Prediction Center  
160 (CPC) (Barnston and Livezey, 1987; Chen and Van den Dool, 2003; Van den Dool et al., 2000).

161 All indices were analyzed at monthly resolution pertaining to the period 2003–2022, to match the SST analysis  
162 period. Prior to correlation and filtering analyses (Section 2.9), each index was standardized (zero mean, unit  
163 variance) over the 2003–2022 period. Provider sign conventions were retained.

164 *Data access notes:* MEI.v2 and the WHWP/TNA indices were retrieved from the NOAA PSL portals; the NAO  
165 index was retrieved from NOAA CPC (accessed in 2024–2025; URLs listed in the Data Availability statement).

## 166 2.5 Statistical analysis

167 All analyses were performed over the domain  $19\text{--}21.75^\circ\text{ N}$ ,  $77\text{--}80^\circ\text{ W}$  (Figure 1). Land points were masked.  
168 Daily fields were aggregated to monthly means, while monthly anomalies were computed by removing the  
169 2003–2022 monthly climatology. Unless otherwise specified, statistics refer to the aforementioned monthly  
170 anomalies.

171 Long-term monthly means were used to show the seasonal cycle of SST and surface heat fluxes (Figures 2–4).  
172 SST frontal zones shown in Figure 2 were identified from local SST differences with a  $\geq 0.5^\circ\text{C}$  threshold and  
173 lightly smoothed with a  $3\times 3$  neighbourhood operator to suppress short wavelength (pixel-scale) noise.

174 To contrast shelf and offshore regimes, the authors computed time series over the two small boxes shown in  
175 Figure 1: GAM (shelf) and CS (oceanic). For each box, monthly anomalies, standard deviations and seasonal  
176 composites were calculated.

177 Linear trends were estimated using ordinary least squares applied to monthly anomalies at each grid point,  
178 separately for each calendar month. Slopes are reported in  $^\circ\text{C}/\text{decade}^{-1}$ . Statistical significance was assessed at



the 95% level using a two-sided t-test with an effective sample size that accounts for autocorrelation in the time series (for example, Thomson and Emery, 2024). To quantify coupling between SST and different drivers, cross-correlations between SST anomalies and net surface heat flux were computed (and, where relevant, horizontal heat advection; Section 2.6) using monthly data, by scanning lags from -6 to +6 months. Reported lags correspond to the peak absolute correlation. Significance was evaluated using the t-test for the correlation coefficient and the effective degrees of freedom approach. Where budget terms are summed (Section 2.6; Figure 5), the uncertainty of the sum was obtained by root-sum-of-squares, assuming weak covariance between terms at monthly resolution. All computations and figure generation were carried out via the MATLAB computing platform using standard scientific libraries.

## 2.6 Mixed-layer heat budget

To identify the processes governing the seasonal variability of SST, the authors applied a standard mixed-layer (ML) heat budget (for example, Moisan and Niiler, 1998). Since the budget is defined in relation to the bulk mixed layer, the GLORYS12 MLT and mixed-layer depth (MLD) were used to ensure physical and numerical consistency among terms (flux  $\rightarrow$  heating rate via  $h$ ; advection using currents acting on the same temperature field). At monthly scales, MUR SST and GLORYS12 MLT were well correlated over the domain (Section 2.2). Therefore, accounting for MLT variability was taken as providing an explanation for the observed SST variability. The prognostic equation for ML temperature  $T$  is

$$\frac{\partial T}{\partial t} = \frac{Q_{\text{net}}}{\rho C_p h} - \mathbf{U} \cdot \nabla T - \frac{(\frac{\partial h}{\partial t} + u_h \nabla h + w_h) \Delta T}{h} + R,$$

where  $\rho = 1025 \text{ kg m}^{-3}$  is seawater density,  $C_p = 3990 \text{ J kg}^{-1} \text{ K}^{-1}$  is the specific heat capacity,  $h$  is the MLD,  $Q_{\text{net}}$  is the net downward surface heat flux (into the ocean,  $\text{W m}^{-2}$ ),  $\mathbf{U} = (U, V)$  is the horizontal current vector representative of the ML,  $w_e$  is the entrainment (positive downward) velocity at the ML base,  $\Delta T = T_{\text{ML}} - T_{\text{below}}$  is the temperature jump across the base of the ML, and  $R$  collects unresolved terms (for example, diffusion, sub-monthly variability and analysis noise). All heating rates are reported in  $^\circ\text{C day}^{-1}$ . Conversion from flux to heating rate follows, whereby

$$1 \text{ W m}^{-2} \equiv \frac{86400}{\rho C_p h} \text{ K day}^{-1},$$

so, for example, with  $h = 20 \text{ m}$ ,  $1 \text{ W m}^{-2} \sim 0.0011^\circ\text{C day}^{-1}$ .



210 All budget terms were computed from daily fields and then averaged to monthly means for analysis and  
211 plots. MLD  $h$  was obtained from GLORYS12 “mixed layer thickness”. This estimate is based on a density  
212 criterion ( $\Delta\sigma_\theta = 0.03 \text{ kg m}^{-3}$ ), following the approach proposed by de Boyer Montégut et al. (2004). Daily  
213 horizontal velocities from GLORYS12 were vertically averaged from the surface to the local ML base,  
214 approximated by thickness-weighted averaging across GLORYS12 levels within the ML.  
215 Surface fluxes ( $Q_{\text{net}}$ ) were estimated from ERA5 shortwave (SW) and longwave (LW) radiation, latent (LHF)  
216 and sensible (SHF) heat fluxes on the  $1/4^\circ$  grid. To reiterate, the authors adopted herein the oceanographic  
217 convention that positive  $Q_{\text{net}}$  warms the ocean:  $Q_{\text{net}} = (\text{SW}\downarrow - \text{SW}\uparrow) + (\text{LW}\downarrow - \text{LW}\uparrow) - \text{LHF} - \text{SHF}$ . The  
218 ERA5 native signs (upward positive for turbulent fluxes) are converted accordingly. Fluxes were bilinearly  
219 remapped to the GLORYS12 grid prior to the application of Equation (1).  
220 Horizontal gradients  $\partial T/\partial x$ ,  $\partial T/\partial y$  were computed with centered finite differences on the GLORYS12 grid. At  
221 a monthly resolution, the flux and advection tendencies in addition to their sum are presented. Furthermore, the  
222 entrainment plus unresolved tendency is treated as a residual (for example, the difference between the observed  
223 monthly MLT tendency and the sum of resolved terms).

## 224 2.7 Marine heatwaves

225 MHWs were detected from daily 1-km MUR SST data, following the hierarchical definition provided by  
226 Hobday et al. (2016, 2018), which contends that an MHW occurs when SST exceeds the seasonally varying  
227 90th percentile threshold for  $\geq 5$  consecutive days. For each grid point, the authors of the present paper computed  
228 a day-of-year (DOY) climatology and corresponding 90th percentile threshold over the period 2003–2022. The  
229 DOY climatology and threshold were formed using a  $\pm 5$ -day moving window in order to smooth sampling  
230 noise. Events were characterized according to their intensity (absolute anomaly relative to the DOY  
231 climatology), duration, frequency, total MHW days and cumulative intensity. MHW categories  
232 (Moderate/Strong/Severe/Extreme) were assigned using the factor-of-rule relative to the local threshold  
233 exceedance (Hobday et al., 2018).

234 All diagnostics were computed per grid cell and subsequently summarized for the sub-regions (GAM and CS,  
235 Figure 1). Figure 8 shows the following: (i) maps pertaining to the mean maximum intensity and total MHW  
236 days (2003–2022); and (ii) an annual time series of the number of events, mean maximum intensity and  
237 maximum category for GAM and CS. It should be noted that the 20-year baseline (2003–2022) used in the  
238 present study corresponds to the period during which 1-km MUR SST data were available. Although shorter  
239 than the conventional 30-year climatology, the present research does, nevertheless, provide consistent  
240 thresholds across the study period.

## 241 2.8 Empirical orthogonal functions

242 The present study used EOFs to extract the dominant space–time patterns of SST variability over the study  
243 domain ( $19\text{--}21.75^\circ \text{ N}$ ,  $77\text{--}80^\circ \text{ W}$ ). The input field was monthly MUR SST anomalies (Section 2.2), i.e.,



244 monthly means with the 2003–2022 monthly climatology removed. Unless otherwise specified, anomalies were  
245 not detrended to ensure that the modes were able to capture the interannual–decadal variability previously  
246 discussed in Section 3.4. It should be noted that a sensitivity test that removed a linear trend produced similar  
247 leading modes (not shown herein). All calculations were performed on the native ~1 km grid. EOFs were  
248 obtained from the covariance matrix of the anomalies, computed via singular-value decomposition. Spatial  
249 patterns (EOFs) were scaled to the unit variance of their associated principal components (PCs) and the fraction  
250 of total variance explained by each mode. The sampling uncertainty of eigenvalues was estimated using North’s  
251 rule of thumb, and whereby modes were treated as distinct when the eigenvalue separation exceeded such  
252 uncertainty. PCs were standardized to zero mean and unit variance; their sign was arbitrary and was chosen so  
253 that positive EOF loadings corresponded to positive PC anomalies during warm events. For correlation analyses  
254 in Section 3.5, both the raw monthly PCs and low-pass filtered PCs were used to isolate variability bands.  
255 Specifically, a 2-year cutoff was employed by the authors to emphasize interannual variability  
256 (ENSO/WHWP/TNA) and a 5-year cutoff for decadal/interdecadal variability (NAO). EOF analysis was carried  
257 out in MATLAB using standard linear-algebra routines.

## 258 **3. Results**

### 259 **3.1 Seasonal cycle and mixed-layer heat budget (GAM vs CS)**

#### 260 **3.1.1 SST and flux climatologies**

261 Monthly SST climatologies (Figure 2) exhibited the expected annual cycles, with boreal summer–early autumn  
262 (August–September) temperatures reaching ~30–33 °C, and winter (January–March) readings dropping to ~22–  
263 26 °C. A pronounced shelf–offshore contrast emerged from November to March, when the GAM/GG shallow  
264 waters are cooler than the adjacent CS, while from April to October this contrast weakened and was virtually  
265 absent in certain months (for example, April and September–October). SST fronts ( $\geq 0.5$  °C) aligned with the  
266 shelf edge and were most frequent/intense during the transition and winter months, consistent with stronger  
267 horizontal gradients at that time.

268 Air–sea flux climatologies (Figure 3) indicated net ocean cooling from October to March and net warming from  
269 April to September. Winter cooling was strongest within the gulf, whereas summer heat peaked near the shelf  
270 break and CS. Cross-correlations between SST and net heat flux reveal a high degree of coupling ( $R^2 \approx 0.6$ –  
271 0.9), with a characteristic lag of ~2 months (flux leads SST), consistent with mixed-layer heat storage. Seasonal  
272 maps of horizontal heat advection (Figure 4) reveal smaller-magnitude, spatially patchy tendencies that warm  
273 during cold months (November–February) and cool during warm months (May–October), thus reflecting the  
274 seasonal reversal of horizontal temperature gradients. Advection effects were most significant along the gulf–  
275 ocean boundary.

276



### 3.1.2 Mixed-layer heat budget for the seasonal cycle

To attribute the seasonal evolution mechanistically, the mixed-layer heat budget (Section 2.6) was applied and GAM and CS were compared (Figure 5). It was found that the air–sea heat-flux tendency  $(\partial T/\partial t)|_Q = Q_{net}/(\rho C_p h)$  dominates the seasonal cycle in both regions. The horizontal advection term  $(\partial T/\partial t)|_{adv} = -U \cdot \nabla T$  is generally an order of magnitude smaller, although it modulates the signal near the shelf edge. The summed tendency (flux + advection) reproduces the observed monthly mixed-layer temperature tendency with a ~2-month lag (flux leads), which confirms that surface heat exchange sets the seasonal cycle, while advection acts in a secondary manner.

Seasonal extremes occur as follows: maximum warming rates from fluxes took place in June–July, and maximum cooling rates occurred in November–December, with stronger magnitudes recorded over GAM in winter and greater summer warming registered nearer to the CS. Advection is more energetic in GAM than in CS (notably during January–June and November–December), which resulted in warming during the cold season and cooling during the warm season. This is consistent with the sign of horizontal SST gradients. The residual (entrainment plus unresolved terms) is small at monthly scales, thus indicating that the flux and advection terms essentially achieve budget closure. It should be noted that the mixed-layer heat budget was applied solely to the seasonal cycle; longer-term variability is addressed in Sections 3.2–3.4 without a heat-budget decomposition.

### 3.2 Interannual variability, long-term trends and the 2011–2013 regime shift

Monthly linear trends of SST anomalies (Figure 6) reveal spatially coherent warming across the domain from 2003 to 2022, with the largest magnitudes occurring in the transition and winter months. Peak grid-point trends occur in April and November, consistent with the domain-mean results, and were more pronounced along the shelf edge compared to offshore waters. Summer trends were weaker and spatially smoother, with local minima in June and July. By conducting stippling, the authors highlight grid cells with  $p < 0.05$  after adjusting for serial autocorrelation. Significant warming dominated most months, particularly from November to March and April. Monthly SST anomalies (Figure 7a,c) show greater variability on the shelf (GAM) than offshore (CS), with standard deviations of  $0.61^\circ\text{C}$  and  $0.41^\circ\text{C}$ , respectively. Several cold winters marked the first half of the record (for example, 2004, 2009, 2011), which were more pronounced in GAM. An additional cold event in 2010 was evident in GAM but weak/absent in CS. In the second decade of study, warm winters predominated (for example, 2014, 2016, 2019, 2020), with stronger occurrences over GAM. Despite not every year conforming to the general trend, results demonstrate an overall evolution that is shifting from predominantly cool to predominantly warm conditions.

Seasonal means by year (Figure 7b,d) confirm that winter (January to March) drives most of the low-frequency change. Piecewise linear fits prior to and after 2011 indicate a winter cooling tendency during 2003–2011, followed by a marked winter warming during 2012–2022. Summer (July to September) warmed throughout the record, albeit with smaller slopes than winter in both regions. The black line in panels (b) and (d) of Figure 7 shows the yearly linear trend, which is positive for both GAM and CS. In conjunction, these patterns indicate a



312 step-like transition from 2011 to 2013 to a persistently warmer state, which is coherent across both shelf and  
313 offshore boxes.

314 In summary, the shelf exhibits larger variance and a stronger wintertime response than the adjacent CS,  
315 consistent with Section 3.1 (shallower mixed layers and stronger air–sea coupling). This transition foreshadows  
316 the increase in marine heatwave activity (Section 3.3) and is consistent with the low-frequency modulation  
317 captured by the EOF analysis (Section 3.4).

### 318 3.3 Marine heatwaves

319 Spatially, the mean of event-wise maximum intensity ranges from  $\sim 1\text{--}2^\circ\text{C}$  across the domain (Figure 8a), with  
320 a regional mean of  $1.3 \pm 0.2^\circ\text{C}$ . Intensities were systematically higher inside the gulf than offshore. Events in  
321 GAM tended to have higher absolute intensity, whereas the CS, which experienced lower background variance,  
322 more often reached higher MHW categories under the Hobday scheme. The total number of MHW days from  
323 2003 to 2022 exceeds 200 at every grid cell and surpasses 400 over most of the GAM (Figure 8b).

324 The year-by-year event calendars for the representative boxes (Figure 8c, d) show broadly similar annual  
325 frequencies in GAM and CS (typically 4–5 events  $\text{yr}^{-1}$ ), with a marked increase in frequency and intensity  
326 during the second decade. The most active period is 2019–2020, followed by 2015–2016, in both regions. The  
327 years 2004 and 2008 are the only ones in which no MHW was detected in either box. Accordingly, a key shelf–  
328 offshore contrast emerges: Events in GAM tended to be more intense, while more high-category events were  
329 registered in the CS; over the entire period, 73 events were recorded in GAM compared to 90 in CS. These  
330 patterns are consistent with the seasonal contrasts established in Section 3.1, i.e., shallow, strongly forced shelf  
331 waters favour larger absolute temperature anomalies (higher intensity), while offshore, the background  
332 threshold and variance regime support more frequent escalation to higher categories.

### 333 3.4 Modes of variability

334 EOFs of monthly SST anomalies (2003–2022) indicate that the first two modes account for 93.7% of the total  
335 variance (EOF1: 87.5%, EOF2: 6.2%) and possess clear physical significance (Figure 9). EOF1 displays a  
336 monopole pattern with positive loadings across the domain, slightly enhanced toward the shelf edge and  
337 offshore. This mode represents coherent warming/cooling of the entire region. Its principal component (PC1)  
338 exhibits low-frequency variability with a pronounced minimum during the 2009–2011 period and positive  
339 excursions in the 2013–2016 and 2019–2020 periods. The 2-year low-pass PC1 highlights the step-like  
340 transition to a warmer state after the 2011–2013 period, consistent with Section 3.2 and with the increase in  
341 MHW activity (Section 3.3).

342 EOF2 is a dipole that opposes the shallow shelf (GAM/GG) to the adjacent CS, with larger amplitudes along  
343 the shelf break. This mode captures differential heating/cooling between coastal and oceanic waters, consistent  
344 with the seasonal mechanisms diagnosed in Section 3.1 (stronger air–sea coupling over the shelf and modulation  
345 by horizontal advection). PC2 fluctuates primarily at interannual timescales, exhibiting alternating  
346 positive/negative phases throughout the period of study, with no persistent trend identified. This indicates



variability that redistributes anomalies between the shelf and offshore regions, rather than warming the entire region.

Overall, EOF1 reflects basin-wide anomalies that underpin the regime shift, whereas EOF2 explains spatial structure related to the shelf–offshore gradient. In Section 3.5, these modes are related to large-scale climate indices in order to assess likely drivers of the interannual–decadal variability.

### 3.5 Climate drivers: EOF PCs vs large-scale indices

The authors of the present paper established a relationship between the leading SST modes and climate variability by comparing PC1/PC2 with standard indices (ENSO [MEI], WHWP, TNA and NAO, Section 2.4) and with domain-mean latent heat flux (LHF, ERA5). Interannual variability was isolated with a 2-year running-mean low-pass, and low-frequency variability with a 5-year running-mean low-pass (zero-lag correlations reported; significance assessed with effective degrees of freedom; Section 2.5).

At interannual scales (Figure 10a), PC1 co-varies with MEI ( $r \approx 0.56$ ), WHWP ( $r \approx 0.58$ ), and especially with LHF ( $r \approx 0.74$ ), consistent with an air–sea heat-flux pathway linking climate modes to regional SST. At low frequencies (Figure 10c), PC1 closely tracks the NAO ( $r \approx 0.90$ ), consistent with the step-like warming observed after 2011–2013 (Section 3.2).

At interannual scales (Figure 10b), PC2 correlates with the TNA index ( $r \approx 0.53$ ), consistent with variability that redistributes anomalies between shelf and offshore rather than producing basin-wide warming. In conjunction, these results indicate that ENSO/WHWP modulates basin-wide anomalies (PC1) via latent heat flux on interannual scales and through the NAO on low-frequency scales. Simultaneously, the shelf–offshore contrast (PC2) is tied to TNA-related variability. Physical mechanisms are discussed in Section 4.

## 4. Discussion

### 4.1 Seasonal mechanisms and shelf–offshore contrast

The mixed-layer heat budget shows that air–sea heat exchange is the primary control on the seasonal evolution of surface temperature across the study area, with horizontal advection acting as a secondary modulator near the shelf break (Section 3.1). This result is entirely consistent with mixed-layer theory and previous diagnostics with regards to tropical–subtropical shelves, where the net surface heat flux drives most of the seasonal tendency, while advection fine-tunes phasing and amplitude (Moisan and Niiler, 1998; de Boyer Montégut et al., 2004). In practice, net surface heat flux accounts for the marked winter cooling (November–March) and summer warming (April–September), whereas advection tends to warm during the cold season and then cool during the warm season, thus reflecting the seasonal reversal of horizontal SST gradients.

The contrast between GAM and the adjacent CS follows directly from this balance. Inside GAM, the mixed layer is shallower, so for any given flux, the temperature tendency ( $\propto Q_{\text{net}}/h$ ) is larger. This explains the faster winter cooling and the enhanced amplitude of the seasonal cycle within the gulf. Along the shelf edge, where



380 SST gradients intensify, the advection term becomes more relevant, and it modulates peaks. Nevertheless, its  
381 magnitude remains smaller than the flux-driven tendency when monthly means are considered. The resulting  
382 picture, in which thermodynamics set the seasonal baseline and circulation provides fine-scale adjustment, is  
383 also consistent with the location and persistence of frontal structures aligned with the shelf break (Figure 2).  
384 These findings support hypothesis 1 of the present study and provide a mechanistic basis for the shelf–offshore  
385 SST contrast described for southern Cuba in previous work (Cerdeira-Estrada et al., 2005; Caravaca et al., 2022;  
386 González-De Zayas et al., 2022).

#### 387 **4.2 Interannual–decadal drivers and 2011–2013 regime shift**

388 Superimposed on the seasonal cycle is a robust long-term warming, which is at its strongest during winter and  
389 transition months and is amplified over the shelf, in line with broader Caribbean tendencies (Avila-Alonso et  
390 al., 2020). The record exhibits a step-like transition between 2011 and 2013, from a relatively cool to a  
391 persistently warmer state, which is coherent throughout GAM and CS. Moreover, the modulation of the  
392 dominant climatic oscillations in the region (NAO, ENSO, WHWP) promotes the progressive accumulation of  
393 heat in the ocean surface layer and its transfer to subsurface levels, which is chiefly responsible for the long-  
394 term warming observed in the area. The EOF analysis clarifies the structure: EOF1 (87.5%) is a basin-wide  
395 mode with positive loadings across the domain and low-frequency fluctuations in PC1; EOF2 (6.2%) is a dipole  
396 which opposes shelf-to-offshore waters and primarily redistributes anomalies without an evident trend.  
397 Relating these modes to large-scale variability (Figure 10) suggests two complementary pathways. At the  
398 interannual scales, PC1 co-varies with ENSO, the WHWP (Wang and Enfield, 2001, 2003; Enfield and Lee,  
399 2005), and most directly with LHF, which is consistent with trade-wind and humidity anomalies that regulate  
400 evaporative cooling over the warm-pool region (Czaja et al., 2002; Wang et al., 2006). The lead–lag structure  
401 (indices leading SST by order of months) favours an air–sea coupling pathway rather than a purely oceanic  
402 origin. At low frequencies, PC1 correlates with the NAO (Hurrell, 1995), which suggests a broader Atlantic  
403 influence on winds and surface heat exchange and, in turn, is consistent with the timing of the 2011–2013  
404 transition. Conversely, PC2 correlates most closely with the TNA index (Enfield et al., 1999), in line with the  
405 differential heating between coastal and oceanic waters and the role of horizontal temperature gradients in  
406 setting advection (Section 3.1). Taken in conjunction, these results support hypotheses 2 and 3 of the present  
407 study: that basin-wide anomalies are largely atmospherically forced through heat-flux pathways linked to  
408 ENSO/WHWP (interannual) and the NAO (low-frequency), whereas the spatial structure within the region  
409 reflects regional thermodynamics and circulation.

#### 410 **4.3 Marine heatwaves: intensity, category and recent escalation**

411 Marine heatwaves increased in frequency and intensity during the second decade, with 2019–2020 being the  
412 most active period, followed by 2015–2016 as the second most active. MHW detection and categorization  
413 follow Hobday et al. (2016, 2018). Relative to the local 90th-percentile threshold, the mean of event-wise  
414 maximum intensity is greater in GAM than offshore, while the total number of MHW days surpasses 400 across



large areas of the gulf. However, the higher category scales (for example, Severe) occur comparatively more often offshore (CS). This contrast is expected under the Hobday scheme, in which categories are defined by the magnitude of local threshold exceedance. Thus, regions with lower background variance can experience higher categories, even for more minor absolute anomalies. Physically, GAM develops larger °C anomalies due to shallow, strongly forced mixed layers, while CS more readily crosses category thresholds owing to tighter local variability.

The warmer background state after the 2011–2013 period effectively preconditions the region for MHW development, increasing both the likelihood and persistence of threshold exceedances. Mechanistically, this links back to Sections 3.1 and 3.5, whereby flux-dominated seasonality sets the baseline and phase, and large-scale atmospheric variability modulates the probability of sustained warm anomalies that seed or prolong events. These patterns echo broader reef-climate concerns in the Caribbean, where rising SSTs and compounding stressors have been associated with bleaching and ecological change (Hughes et al., 2003; Bruno et al., 2019; Cramer et al., 2020; van Hooidonk et al., 2015), including at JRNP and neighbouring MPAs (Pina Amargós et al., 2011; Hernández-Fernández et al., 2011, 2016, 2019a; Gerhartz-Muro et al., 2018; Caballero-Aragón et al., 2020).

#### 4.4 Limitations, assumptions and robustness

Several methodological choices bound the interpretation. The budget is formulated for the bulk mixed layer and, as a consequence, the authors of the present study used GLORYS12 mixed-layer temperature, depth and currents for internal consistency among terms, by computing all tendencies on a daily basis and averaging these to monthly values. MUR SST was reserved for descriptive and MHW analyses. At monthly scales, MLT and SST are well correlated; however, residual differences may persist at daily scales due to skin effects and diurnal warming.

ERA5 and GLORYS12 may exhibit coastal biases. Particularly, it was not possible to directly evaluate the realism of GLORYS12 currents in the gulfs or the adjacent CS because no in-situ velocity observations (for example, those undertaken by Acoustic Doppler Current Profiler moorings or high-frequency radars) were available for the study period. This is a non-trivial caveat: reproducing circulation in highly shallow, embayed shelves, such as the GAM and the GG, is notoriously challenging for global reanalyses. This is because the effective  $1/12^\circ$  (~8–9 km) resolution and required bathymetric smoothing under-resolve narrow channels, weak pressure-gradient flows and small eddies. Moreover, the abrupt depth changes along the shelf break and the roughness and enhanced bottom friction associated with coral-reef frameworks further challenge the representation by the model of nearshore dynamics. Accordingly, the advective term in the mixed-layer budget herein should be interpreted as a conservative lower bound, which captures sign and seasonality but, potentially, underestimates magnitudes close to the coast. Targeted in-situ current measurements and/or nested higher-resolution regional modelling would help refine the role of advection within the gulfs.

Trends and correlations account for serial autocorrelation through effective degrees of freedom. EOFs were analyzed from raw data as well as from data to which 2-year and 5-year low-pass filters were applied. While



451 filtering choices can shift correlation maxima to a certain degree, they do not alter the physical interpretation.  
452 The 1-km MUR record dictates the 20-year baseline (2003–2022) and is shorter than the canonical 30-year  
453 climatology. Thresholds and category counts may therefore be modestly sensitive to baseline choice; extending  
454 thresholds with longer-record products (for example, coarser-resolution SST) would represent a more thorough  
455 sensitivity check.  
456 Overall, such limitations do not alter the headline result: that surface heat flux dominates the seasonal cycle,  
457 that basin-wide anomalies are atmospherically forced, and that shelf–offshore contrasts arise from the interplay  
458 of mixed-layer depth and horizontal gradients.

#### 459 **4.5 Implications for JRNP and outlook**

460 Two immediate implications follow. First, the strong coupling between net heat flux and temperature, in  
461 conjunction with the typical ~two-month lag, suggest that simple seasonal outlooks based on forecasts of  
462 radiative and turbulent fluxes and mixed-layer depth could offer early warning of forthcoming warming or  
463 cooling within GAM. Second, routine tracking of ENSO/WHWP (interannual) and NAO (low-frequency)  
464 provides a large-scale context for risk assessment. Consequently, positive phases aligned with reduced latent-  
465 heat loss increase the likelihood of basin-wide warmth (PC1) and, consequently, of MHW occurrence and  
466 persistence.

467 Moving forward, the following aspects have the potential to directly contribute to improving knowledge and  
468 forecasting capacity in the region: (a) in-situ observation of currents and conductivity, temperature and depth  
469 (from moorings or gliders transects) within JRNP and across the shelf break; (b) extended MHW climatologies,  
470 for example, by deriving thresholds from longer-record SST products, while retaining MUR for spatial detail;  
471 (c) targeted analyses of regional circulation features, such as shelf-break jets or eddy interactions, that may  
472 enhance advection during transition seasons at the local level; and (d) a practical next step is to implement a  
473 regional, high-resolution ocean model (for example, CROCO) nested in GLORYS12/ERA5 and tailored to the  
474 JRNP–GAM–GG system. A horizontal resolution of ~1 km or finer (with tidal forcing, realistic bathymetry/reef  
475 roughness and bulk fluxes) would enhance efforts to resolve shelf-break jets, gulf exchanges and frontal  
476 dynamics that are under-represented in global reanalyses. Such steps would not only consolidate the  
477 mechanistic framework presented herein, but also help to translate it into operational guidance for conservation  
478 and management within the national park.

#### 479 **5. Conclusions**

480 The present study has quantified seasonal-to-decadal variability of sea-surface temperature (SST) in and around  
481 the Jardines de la Reina National Park (JRNP), with the primary objective to identify the mechanisms and  
482 climate drivers that shape this variability, using daily 1-km MUR SST (2003–2022), ERA5 surface fluxes and  
483 GLORYS12 mixed-layer fields.



484 A mixed-layer heat budget shows that net surface heat flux sets the seasonal evolution of SST, with horizontal  
485 advection providing a smaller modulation near the shelf break; a characteristic ~2-month lead of flux over  
486 temperature is consistent with mixed-layer heat storage and explains the enhanced winter cooling and stronger  
487 thermal gradients along the shelf edge. A clear shelf–offshore contrast emerges: the shallow gulfs (GAM/GG)  
488 markedly differ from the adjacent Caribbean Sea (CS) in autumn–winter (November–March), whereas  
489 conditions during spring–summer are comparatively homogeneous. This reflects shallower mixed layers and  
490 greater flux sensitivity inside the gulfs, with advection adding local modulation. Superimposed on this baseline  
491 is a warming trend of  $\sim 0.28^{\circ}\text{C}/\text{decade}^{-1}$  (2003–2022), which is strongest in winter and transition months, with  
492 monthly maxima around April ( $\sim 0.48^{\circ}\text{C}/\text{decade}^{-1}$ ) and November ( $\sim 0.35^{\circ}\text{C}/\text{decade}^{-1}$ ), and a step-like transition  
493 in 2011–2013 towards a persistently warmer state. The warming trend is predominantly driven by the phase  
494 shift of the NAO, since the study period begins in a negative phase and ends in a positive phase. In addition,  
495 the interannual to decadal modulation of other dominant climatic oscillations in the region (ENSO, WHWP),  
496 in conjunction with latent heat fluxes, favours the progressive accumulation of heat in the ocean surface layer.  
497 Marine heatwaves intensified during the second decade (with the 2019–2020 period the most active, followed  
498 by 2015–2016). Mean event-wise maximum intensity is higher within GAM, whereas upper categories occur  
499 relatively more often offshore, consistent with lower background variance in the area, while total MHW days  
500 exceed 200 across the domain and 400 over much of the gulf. EOFs separate a basin-wide mode (EOF1, 87.5%),  
501 co-varying interannually with ENSO/WHWP and latent-heat flux and at low frequencies with the NAO, from  
502 a shelf–offshore dipole (EOF2, 6.2%) linked most clearly to TNA. This indicates atmospheric forcing of basin-  
503 wide anomalies with regional thermodynamics and advection setting spatial structure.  
504 Practically, seasonal outlooks based on forecasts of net heat flux and mixed-layer depth, in addition to routine  
505 monitoring of ENSO/WHWP and NAO, can help to inform MHW risk in relation to JRNP. Indeed, a regional  
506 high-resolution ocean model (for example, ROMS/CROCO at ~1 km or finer), combined with targeted in-situ  
507 observations, would further improve prediction and attribution. In conjunction, the results of the present  
508 research provide a physically grounded baseline for anticipating future thermal stress and for guiding  
509 conservation and management efforts within JRNP in response to continued climate warming.  
510



511 **Code and data availability:**

512 The data supporting the findings of this study are openly available from public repositories. Sea surface  
513 temperature data from the MUR dataset can be accessed at the JPL Physical Oceanography Distributed Active  
514 Archive Center (PODAAC, <https://podaac.jpl.nasa.gov>). The GLORYS12 ocean reanalysis data used are  
515 available through the Copernicus Marine Environment Monitoring Service (<https://marine.copernicus.eu>).  
516 ERA5 reanalysis data can be obtained from the European Centre for Medium-Range Weather Forecasts  
517 Climate Data Store (<https://cds.climate.copernicus.eu>). All processed data and analysis scripts are referenced  
518 in the manuscript and are available upon reasonable request.

519 **Author contribution:**

520 MC conceived the original idea, performed data analysis and image visualization and was responsible for  
521 writing the manuscript. OP co-conceived the original idea, helped interpret the results and provided key input  
522 in discussions and further writing. He also served as supervisor. AM contributed with the preparation of the  
523 original idea and conducted a review of the results and discussions. He was co-supervisor. IPS undertook data  
524 analysis and result interpretation and played a key role in discussions pertaining to heat balance. DC  
525 performed analysis of the MHWs and heat balance and supported the writing and interpretation of the results  
526 and discussions. DB endorsed the analysis and interpretation of SST trends and assisted in reviewing the  
527 manuscript. LC provided support with image processing using the geographic information system (QGIS).

528 **Competing interests:**

529 The authors declare no conflicts of interest.

530 **Acknowledgements:**

531 The authors wish to thank the reviewers for their comments, which contributed significantly to the  
532 improvement of the quality of the manuscript. They are grateful to all collaborators and institutions that  
533 contributed to the preparation of the present manuscript. They also acknowledge the financial support of  
534 various national and international funding agencies. We used Grammarly, DeepL, and MS Word corrector  
535 during the writing of the manuscript.

536 **Financial support:**

537 This research was supported by the National Agency for Research and Development of Chile (ANID), Grant  
538 21211088 for the PhD in Oceanography at the Universidad de Concepción and partially funded by the  
539 Chilean Millennium Institute of Oceanography (IMO) (grant IC-120019) and the postgraduate department of  
540 the Universidad de Concepción. Iván Pérez-Santos was funded by COPAS COASTAL (ANID FB210021)  
541 and FONDECYT 1251038. OP thanks support from FONDECYT 1241203.



542 **References**

- 543 Appeldoorn, R. S. and Lindeman, K. C.: A Caribbean-wide survey of marine reserves: spatial coverage and  
544 attributes of effectiveness, *Gulf and Caribbean Research*, 14, 139–154, 2003.
- 545 Arriaza, L., Simanca, J., Rodas, R., Lorenzo, S., Hernández, M., Linares, E. O., Milian, D., and Romero, P.:  
546 Corrientes marinas estimadas en la plataforma suroriental cubana, *Serie Oceanológica*, 4, 1-10, 2008.
- 547 Avila-Alonso, D., Baetens, J. M., Cardenas, R., and De Baets, B.: Spatio-temporal variability of oceanographic  
548 conditions in the Exclusive Economic Zone of Cuba, *Journal of Marine Systems*, 212, 103416, 2020.
- 549 Barnston, A. G. and Livezey, R. E.: Classification, seasonality and persistence of low-frequency atmospheric  
550 circulation patterns, *Monthly Weather Review*, 115, 1083–1126, 1987.
- 551 Bruno, J. F., Côté, I. M., and Toth, L. T.: Climate change, coral loss, and the curious case of the parrotfish  
552 paradigm: why don't marine protected areas improve reef resilience?, *Annual Review of Marine Science*, 11,  
553 307–334, 2019.
- 554 Caballero-Aragón, H., Perera-Valderrama, S., Rey-Villiers, N., González-Méndez, J., and Armenteros, M.:  
555 Population status of *Acropora palmata* (Lamarck, 1816) in Cuban coral reefs, *Regional Studies in Marine*  
556 *Science*, 34, 101029, <https://doi.org/10.1016/j.rsma.2019.101029>, 2020.
- 557 Caravaca, A. M., Torres, L. C., and Alfonso, L. V.: Sea Surface Temperature Trends in the Southern Cuban  
558 Shelves for the Period 1982–2018, *Cham*, 81-90, 2022.
- 559 Cerdeira-Estrada, S., Müller-Karger, F. E., and Gallegos-García, A.: Variability of the sea surface temperature  
560 around Cuba, *Gulf of Mexico Science*, 23, 2, 2005.
- 561 Chang, Y.-L. and Oey, L.-Y.: Coupled response of the trade wind, SST gradient, and SST in the Caribbean Sea,  
562 and the potential impact on Loop Current's interannual variability, *Journal of Physical Oceanography*, 43,  
563 1325–1344, 2013.
- 564 Chen, H. C., Jin, F.-F., and Jiang, L.: The phase-locking of tropical North Atlantic and the contribution of  
565 ENSO, *Geophysical Research Letters*, 48, e2021GL095610, 2021.
- 566 Chen, W. Y. and Van den Dool, H.: Sensitivity of teleconnection patterns to the sign of their primary action  
567 center, *Monthly Weather Review*, 131, 2885–2899, 2003.
- 568 Chin, T. M., Vazquez-Cuervo, J., and Armstrong, E. M.: A multi-scale high-resolution analysis of global sea  
569 surface temperature, *Remote Sensing of Environment*, 200, 154–169, <https://doi.org/10.1016/j.rse.2017.07.029>,  
570 2017.
- 571 Chollett, I., Mumby, P. J., Müller-Karger, F. E., and Hu, C.: Physical environments of the Caribbean Sea,  
572 *Limnology and Oceanography*, 57, 1233–1244, 2012.
- 573 Cook, K. and Vizy, E.: Hydrodynamics of the Caribbean low-level jet and its relationship to precipitation,  
574 *Journal of Climate*, 23, 1477–1494, 2010.
- 575 Cramer, K. L., Jackson, J. B. C., Donovan, M. K., Greenstein, B. J., Korpanty, C. A., Cook, G. M., and Pandolfi,  
576 J. M.: Widespread loss of Caribbean acroporid corals was underway before coral bleaching and disease  
577 outbreaks, *Science Advances*, 6, eaax9395, <https://doi.org/10.1126/sciadv.aax9395>, 2020.
- 578 Czaja, A., Van der Vaart, P., and Marshall, J.: A diagnostic study of the role of remote forcing in tropical  
579 Atlantic variability, *Journal of Climate*, 15, 3280–3290, 2002.



- 580 de Boyer Montégut, C., Madec, G., Fischer, A. S., Lazar, A., and Iudicone, D.: Mixed layer depth over the  
581 global ocean: An examination of profile data and a profile-based climatology, *Journal of Geophysical Research:*  
582 *Oceans*, 109, 2004.
- 583 Emilsson, I. and Tápanes, J. J.: Contribución a la hidrología de la plataforma sur de Cuba, *Serie Oceanológica*,  
584 9, 1971.
- 585 Enfield, D. B. and Lee, S.-K.: The heat balance of the Western Hemisphere warm pool, *Journal of Climate*, 18,  
586 2662–2681, 2005.
- 587 Enfield, D. B., Mestas-Núñez, A. M., Mayer, D. A., and Cid-Serrano, L.: How ubiquitous is the dipole  
588 relationship in tropical Atlantic sea surface temperatures?, *Journal of Geophysical Research: Oceans*, 104,  
589 7841–7848, 1999.
- 590 Fernández, L. H. and López, C. B.: Condición de la población de ACROPORA PALMATA LAMARCK, 1816  
591 en arrecifes del Parque Nacional Jardines de la Reina, Cuba, *Revista de Investigaciones Marinas*, 37, 2017.
- 592 Gerhartz-Muro, J. L., Kritzer, J. P., Gerhartz-Abraham, A., Miller, V., Pina-Amargós, F., and Whittle, D.: An  
593 evaluation of the framework for national marine environmental policies in Cuba, *Bulletin of Marine Science*,  
594 94, 443–459, 2018.
- 595 González-De Zayas, R., Pupo, F. M., González, J. A. L., and Hernández-Fernández, L.: Temporal behavior of  
596 air and sea surface temperature in a marine protected area of Cuba: the Jardines de la Reina National Park,  
597 *Holos Environment*, 22, 46–64, 2022.
- 598 Graham, N. A. J., Jennings, S., MacNeil, M. A., Mouillot, D., and Wilson, S. K.: Predicting climate-driven  
599 regime shifts versus rebound potential in coral reefs, *Nature*, 518, 94–97, 2015.
- 600 Hernández-Fernández, L., González de Zayas, R., Olivera, Y. M., Pina Amargós, F., Bustamante López, C.,  
601 Dulce Sotolongo, L. B., Bretos, F., Figueredo Martín, T., Lladó Cabrera, D., and Salmón Moret, F.: Distribution  
602 and status of living colonies of *Acropora* spp. in the reef crests of a protected marine area of the Caribbean  
603 (Jardines de la Reina National Park, Cuba), *PeerJ*, 7, e6470, 2019.
- 604 Hernández-Fernández, L., Guimaraes Bermejo, M., Arias Barreto, R., and Clero Alonso, L.: Composición de  
605 las comunidades de octocorales y corales pétreos y la incidencia del blanqueamiento del 2005 en Jardines de la  
606 Reina, Cuba, *Journal of Marine and Coastal Sciences*, 3, 77–90, 2011.
- 607 Hobday, A. J., Alexander, L. V., Perkins, S. E., Smale, D. A., Straub, S. C., Oliver, E. C. J., Benthuisen, J. A.,  
608 Burrows, M. T., Donat, M. G., and Feng, M.: A hierarchical approach to defining marine heatwaves, *Progress*  
609 *in Oceanography*, 141, 227–238, 2016.
- 610 Hobday, A. J., Oliver, E. C. J., Sen Gupta, A., Thomas, L., and Benthuisen, J. A.: Categorizing and naming  
611 marine heatwaves, *Oceanography*, 31(2), 162–173, 2018.
- 612 Hughes, T. P., Baird, A. H., Bellwood, D. R., Card, M., Connolly, S. R., Folke, C., Grosberg, R., Hoegh-  
613 Guldberg, O., Jackson, J. B. C., and Kleypas, J.: Climate change, human impacts, and the resilience of coral  
614 reefs, *Science*, 301, 929–933, 2003.
- 615 Hurrell, J. W.: Decadal trends in the North Atlantic Oscillation: regional temperatures and precipitation,  
616 *Science*, 269, 676–679, 1995.
- 617 Jackson, J., Donovan, M., Cramer, K., and Lam, V.: Status and trends of Caribbean coral reefs: 1970–2012,  
618 *Global Coral Reef Monitoring Network (GCRMN)*, IUCN, Gland, Switzerland, 2014.



- 619 Kumagai, N. H. and Yamano, H.: High-resolution modelling of thermal thresholds and environmental  
620 influences on coral bleaching for local and regional reef management, *PeerJ*, 6, e4382, 2018.
- 621 Linton, D., Smith, R., Alcolado, P., Hanson, C., Edwards, P., Estrada, R., Fisher, T., Fernandez, R. G., Geraldles,  
622 F., and McCoy, C.: 15. Status of coral reefs in the northern Caribbean and Atlantic node of the GCRMN, in:  
623 Status of Coral Reefs of the World: 2002, Australian Institute of Marine Science; Global Coral Reef Monitoring  
624 Network, 277-302, 2002.
- 625 Lotze, H. K., Lenihan, H. S., Bourque, B. J., Bradbury, R. H., Cooke, R. G., Kay, M. C., Kidwell, S. M., Kirby,  
626 M. X., Peterson, C. H., and Jackson, J. B. C.: Depletion, degradation, and recovery potential of estuaries and  
627 coastal seas, *Science*, 312, 1806–1809, 2006.
- 628 Moisan, J. R. and Niiler, P. P.: The seasonal heat budget of the North Pacific: net heat flux and heat storage  
629 rates (1950–1990), *Journal of Physical Oceanography*, 28, 401–421, 1998.
- 630 Mumby, P. J., Flower, J., Chollett, I., Box, S. J., Bozec, Y.-M., Fitzsimmons, C., Forster, J., Gill, D., Griffith-  
631 Mumby, R., and Oxenford, H. A.: Towards reef resilience and sustainable livelihoods: a handbook for  
632 Caribbean coral reef managers, University of Exeter, Exeter, 2014.
- 633 Pérez-Santos, I., Schneider, W., Sobarzo, M., Montoya-Sánchez, R., Valle-Levinson, A., and Garcés-Vargas,  
634 J.: Surface wind variability and its implications for the Yucatán Basin–Caribbean Sea dynamics, *Journal of*  
635 *Geophysical Research: Oceans*, 115, C10052, 2010.
- 636 Skerrett, F., Adelson, A., and Collin, R.: Performance of high-resolution MUR satellite sea surface temperature  
637 data as a proxy for near-surface in situ temperatures on neotropical reefs, *Latin American Journal of Aquatic*  
638 *Research*, 52, 270–288, 2024.
- 639 Thomson, R. E. and Emery, W. J.: *Data Analysis Methods in Physical Oceanography*, 4th edn., Elsevier,  
640 Amsterdam, 2024.
- 641 Van den Dool, H., Saha, S., and Johansson, A.: Empirical orthogonal teleconnections, *Journal of Climate*, 13,  
642 1421–1435, 2000.
- 643 van Hooijdonk, R., Maynard, J. A., Liu, Y., and Lee, S. K.: Downscaled projections of Caribbean coral bleaching  
644 that can inform conservation planning, *Global Change Biology*, 21, 3389–3401, 2015.
- 645 Venegas, R. M., Acevedo, J., and Treml, E. A.: Three decades of ocean warming impacts on marine ecosystems:  
646 a review and perspective, *Deep-Sea Research Part II: Topical Studies in Oceanography*, 212, 105318, 2023.
- 647 Waliser, D. and Jiang, X.: Tropical meteorology and climate: Intertropical Convergence Zone, *Encyclopedia of*  
648 *atmospheric sciences*, 6, Elsevier, 121-131, 2015.
- 649 Wang, C. and Enfield, D. B.: The tropical Western Hemisphere warm pool, *Geophysical Research Letters*, 28,  
650 1635–1638, 2001.
- 651 Wang, C. and Enfield, D. B.: A further study of the tropical Western Hemisphere warm pool, *Journal of Climate*,  
652 16, 1476–1493, 2003.
- 653 Wang, C., Enfield, D. B., Lee, S.-K., and Landsea, C. W.: Influences of the Atlantic warm pool on Western  
654 Hemisphere summer rainfall and Atlantic hurricanes, *Journal of Climate*, 19, 3011–3028, 2006.
- 655 Wang, C., Lee, S.-K., and Enfield, D. B.: Impact of the Atlantic warm pool on the summer climate of the  
656 Western Hemisphere, *Journal of Climate*, 20, 5021–5040, 2007.



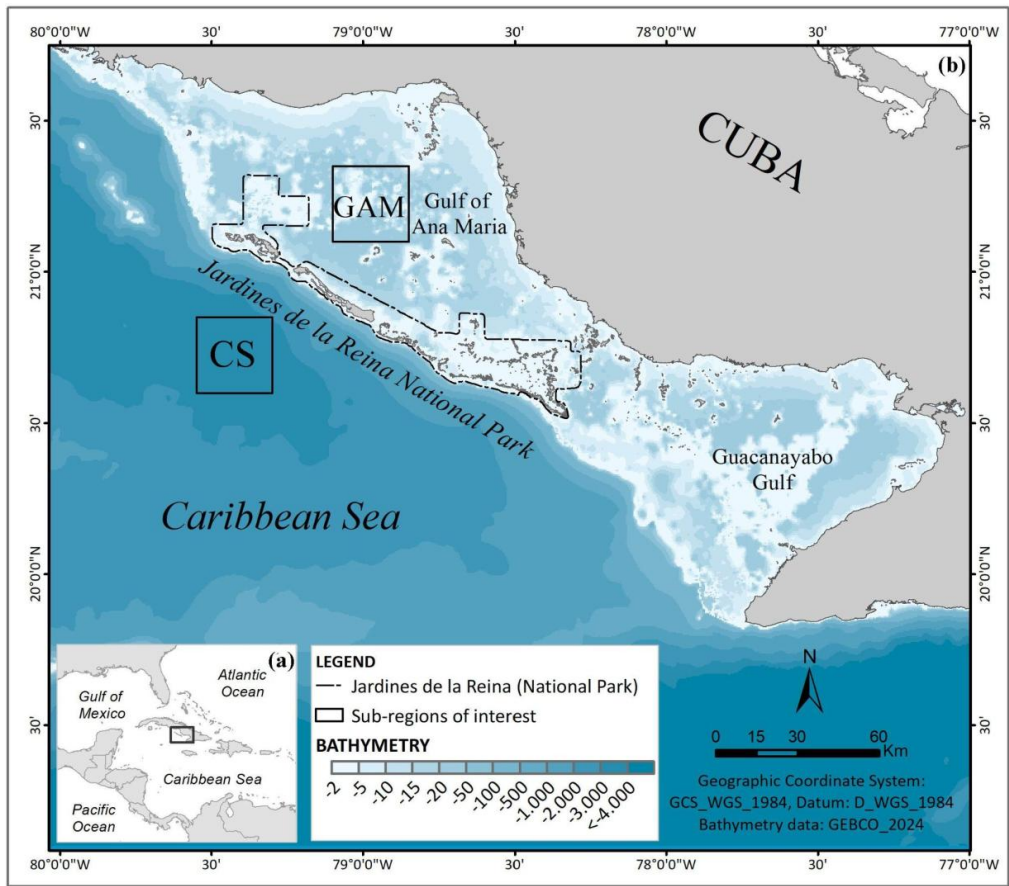
657 Wolter, K.: Monitoring ENSO in COADS with a seasonally adjusted principal component index, in:  
658 Proceedings of the 17th Climate Diagnostics Workshop, 1993.

659 Zhang, T., Hoell, A., Perlwitz, J., Eischeid, J., Murray, D., Hoerling, M., and Hamill, T. M.: Towards  
660 probabilistic multivariate ENSO monitoring, *Geophysical Research Letters*, 46, 10532–10540, 2019.

661



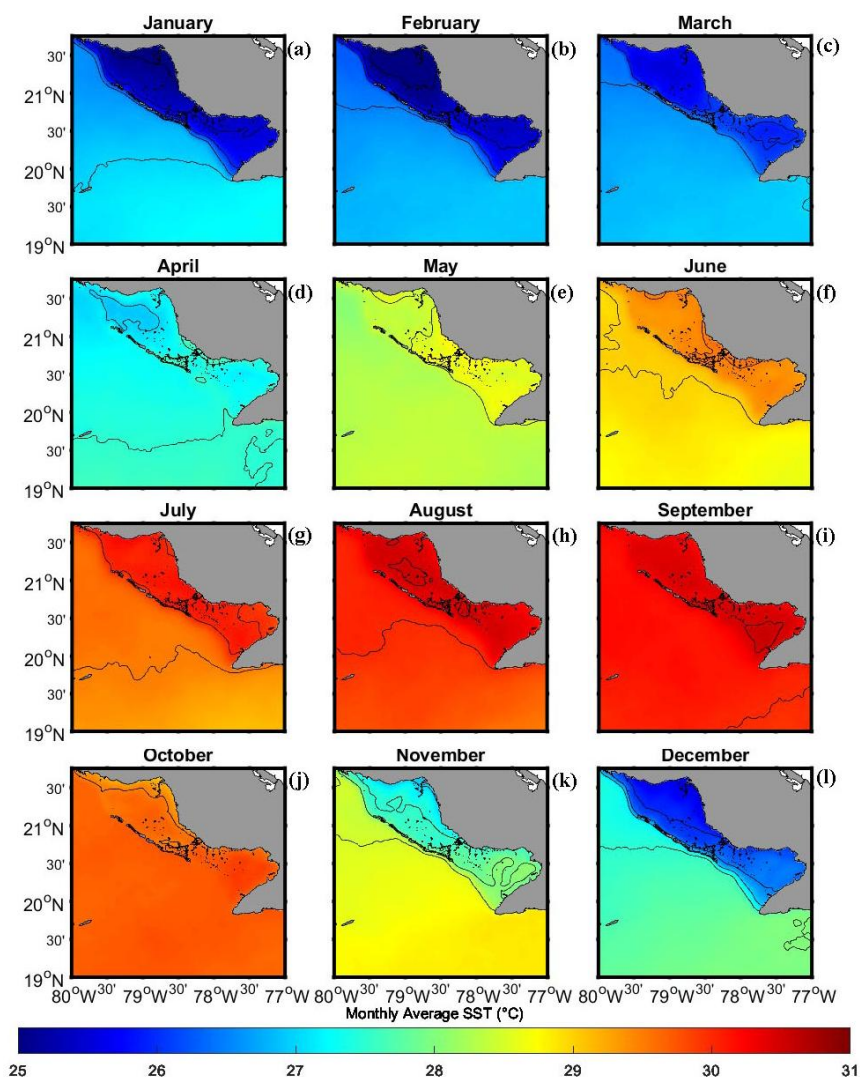
662 **Figures**



663  
664 **Figure 1.** Study area and sub-regions. (a) Regional setting: Cuba in the Caribbean Sea (CS), with the study  
665 domain indicated by the black rectangle. (b) Southeastern Cuban shelf showing the Jardines de la Reina National  
666 Park (black polygon) and neighbouring gulfs: Gulf of Ana María (GAM) and Gulf of Guacanayabo (GG). Black  
667 boxes mark the two analysis sub-regions: GAM (shelf) and CS (oceanic). Colour shading shows bathymetry  
668 (m) from GEBCO\_2024.  
669



670



671

672

673

674

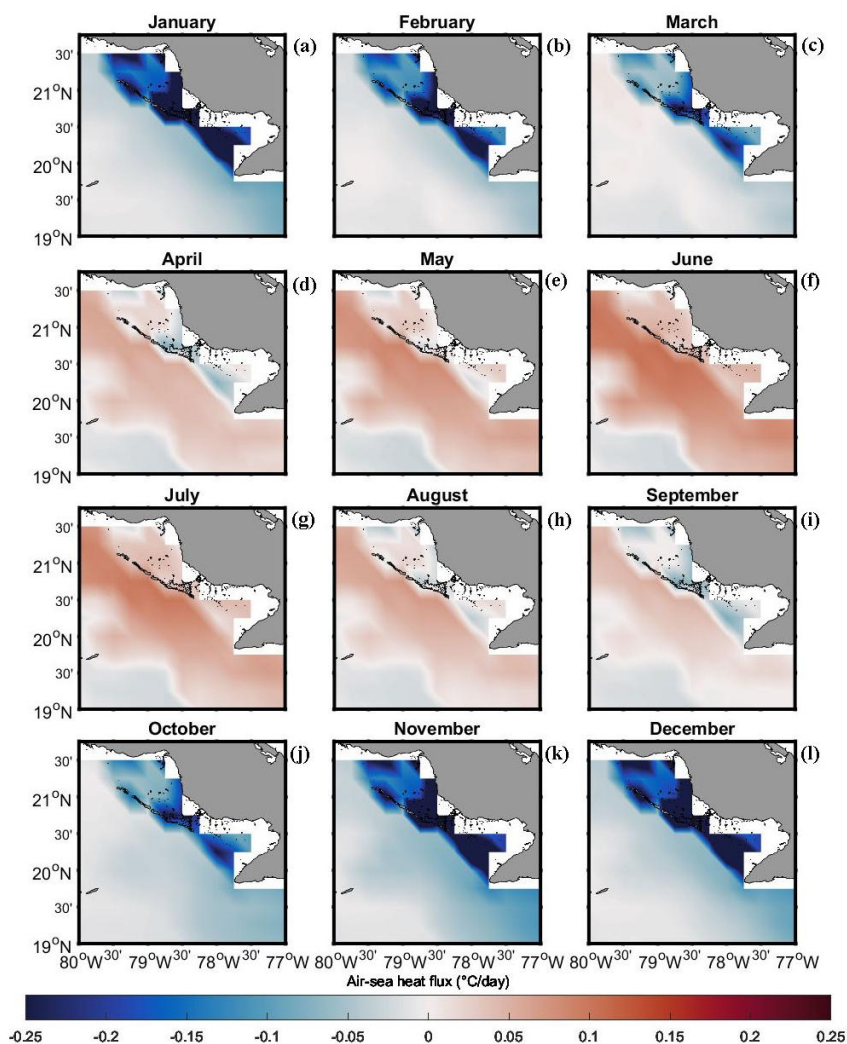
675

676

**Figure 2.** Monthly SST climatology (2003–2022). Panels (a–l) show monthly mean sea-surface temperature (°C) from January to December. Black contours mark SST fronts identified, where local horizontal SST differences are  $\geq 0.5$  °C. Seasonal groupings are: (a–c) boreal winter (JFM), (d–f) spring (AMJ), (g–i) summer (JAS), and (j–l) autumn (OND). The colour bar indicates monthly mean SST (°C); land is masked in grey.



677



678

679

680

681

682

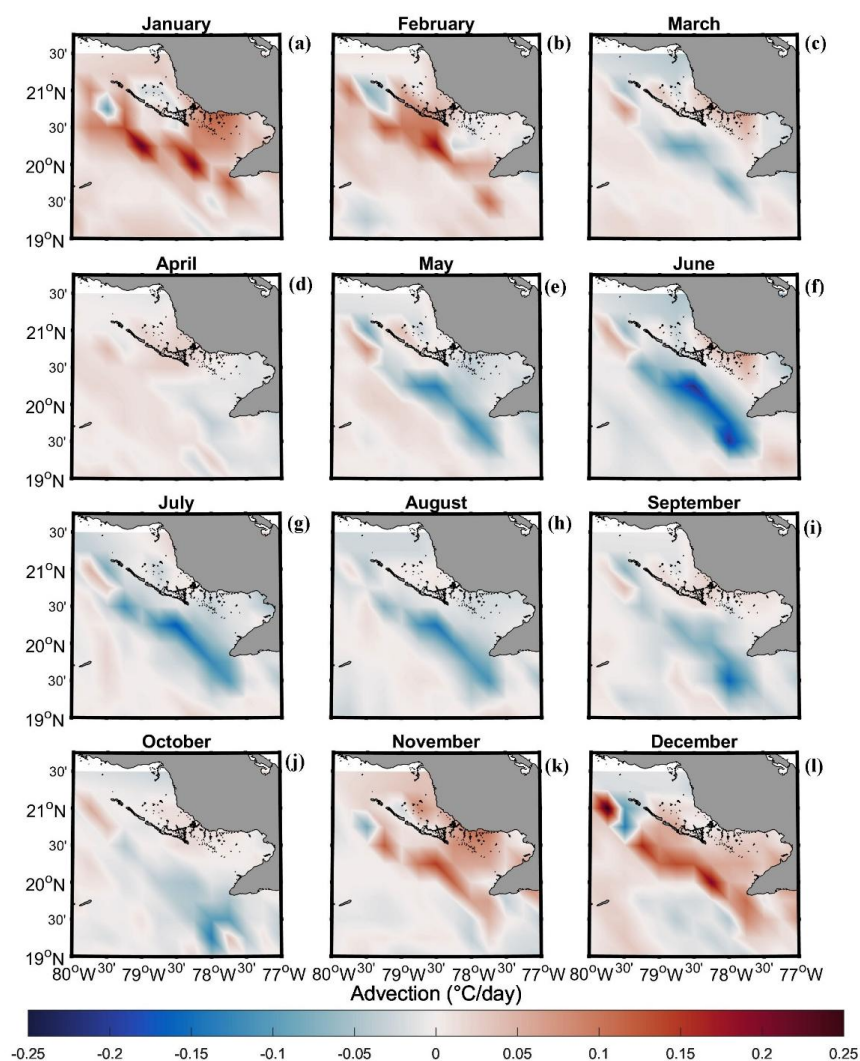
683

684

**Figure 3.** Monthly air–sea heat-flux tendency (2003–2022). Panels (a–l) show the monthly mean mixed-layer heating rate due to net air–sea heat exchange, expressed as  $^{\circ}\text{C day}^{-1}$  and computed as  $(\partial T/\partial t)|_Q = Q_{\text{net}}/(\rho C_p h)$ . Positive (red) warms the ocean; negative (blue) cools the ocean. Months run January–December; seasonal groupings are (a–c) boreal winter (JFM), (d–f) spring (AMJ), (g–i) summer (JAS), and (j–l) autumn (OND). Flux components are from ERA5, mixed-layer depth  $h$  from GLORYS12; land is masked in grey.



685



686

687

688

689

690

691

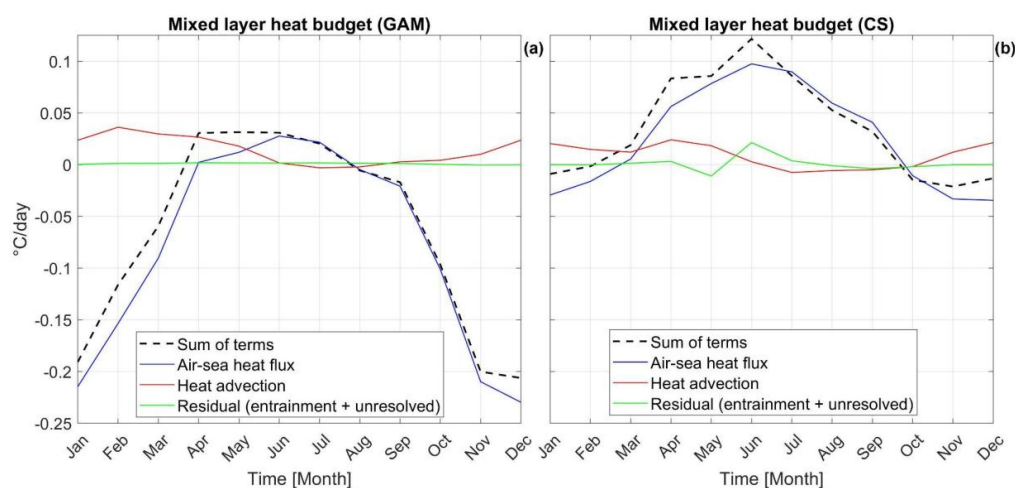
692

693

**Figure 4.** Monthly horizontal heat-advection tendency (2003–2022). Panels (a–l) show the monthly mean mixed-layer temperature tendency due to horizontal advection, expressed as  $^{\circ}\text{C day}^{-1}$  and computed as  $(\partial T / \partial t)|_{adv} = -U \cdot \nabla T$ . Positive (red) warms the mixed layer; negative (blue) cools it. Currents and temperature gradients are from GLORYS12 (ML-averaged currents and mixed-layer temperature); land is masked in grey.



694



695

696

697

698

699

700

701

702

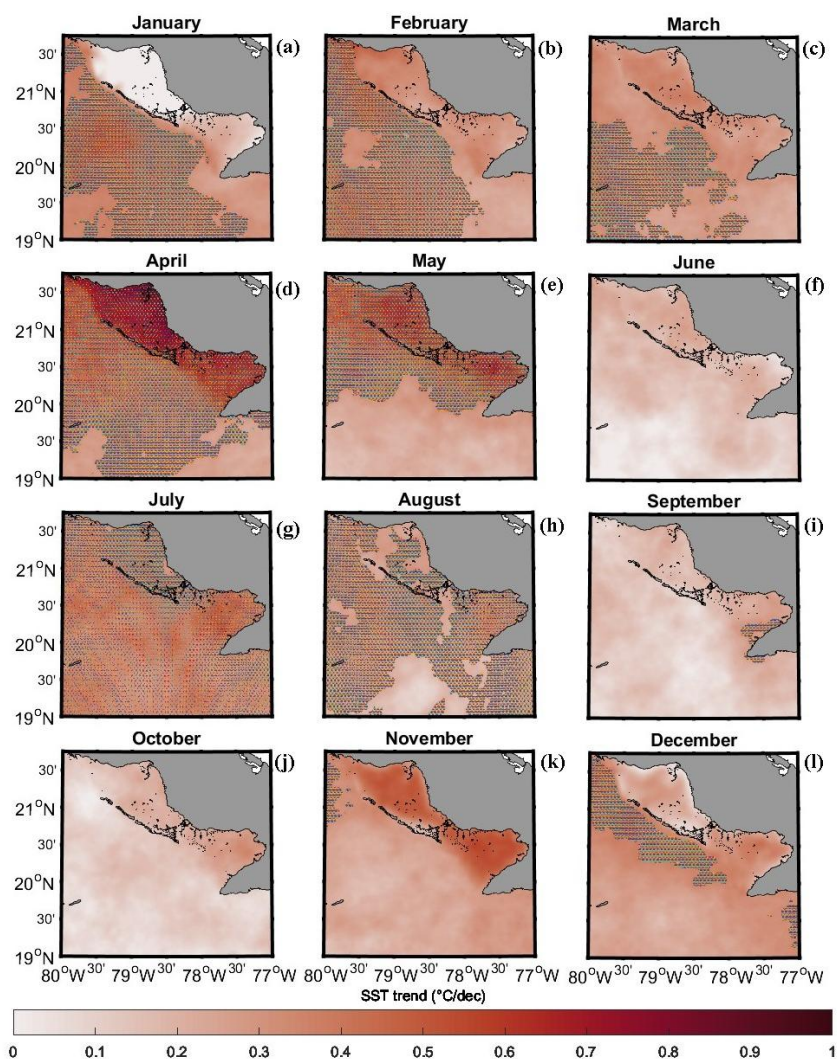
703

704

**Figure 5.** Seasonal mixed-layer heat budget (2003–2022). Monthly climatologies of mixed-layer temperature tendencies ( $^{\circ}\text{C day}^{-1}$ ) for (a) GAM and (b) CS. Blue line: air–sea heat-flux tendency  $(\partial T/\partial t)|_Q = Q_{net}/(\rho C_p h)$ . Red line: horizontal advection  $(\partial T/\partial t)|_{adv} = -U \cdot \nabla T$ . Dashed black line: sum of resolved terms (flux + advection). Green line: residual (entrainment + unresolved processes), computed as the observed mixed-layer temperature tendency minus the sum of resolved terms. Positive values warm the mixed layer; negative values cool it. All terms were computed from daily fields and averaged to monthly means; see Section 2.6 for data sources and sign conventions.



705



706

707

708

709

710

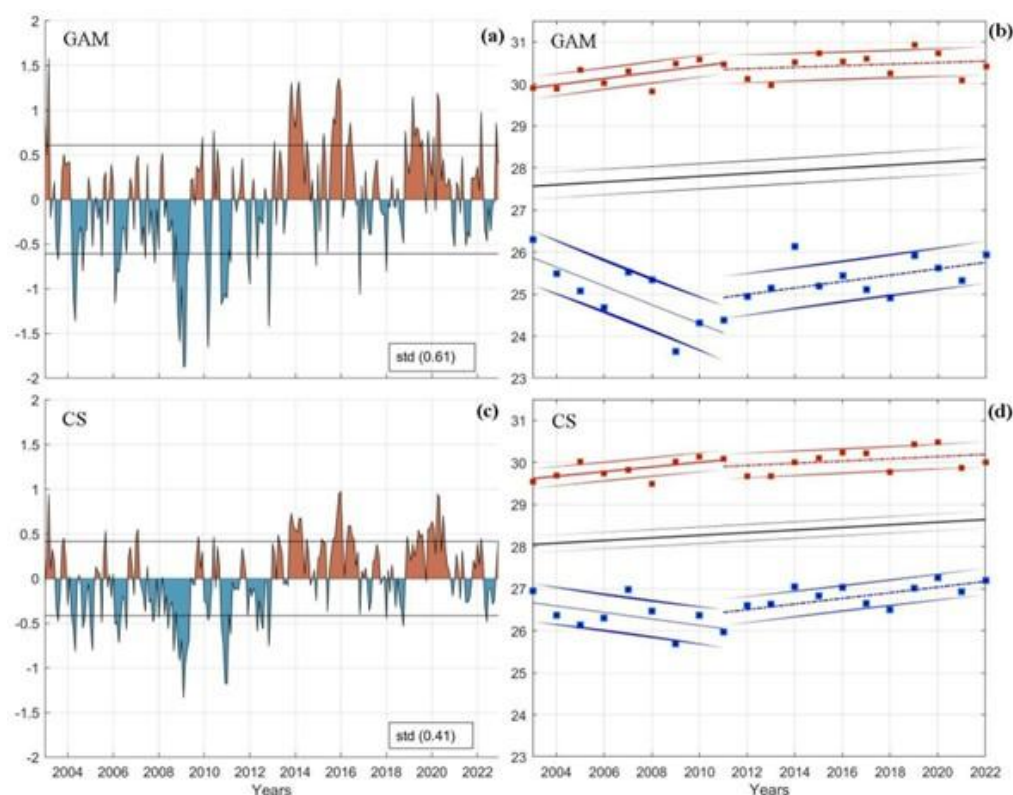
711

712

**Figure 6.** Monthly SST trends (2003–2022). Linear trends of monthly SST anomalies ( $^{\circ}\text{C decade}^{-1}$ ) for January–December (panels a–l). Trends are estimated by ordinary least squares applied to monthly anomalies at each grid point. Stippling indicates grid cells that are significant at the 95% level (two-sided t-test), using effective degrees of freedom to account for autocorrelation. Warming intensifies in winter and transition months, with maxima in April and November; land is masked in grey.



713



714

715

716

717

718

719

720

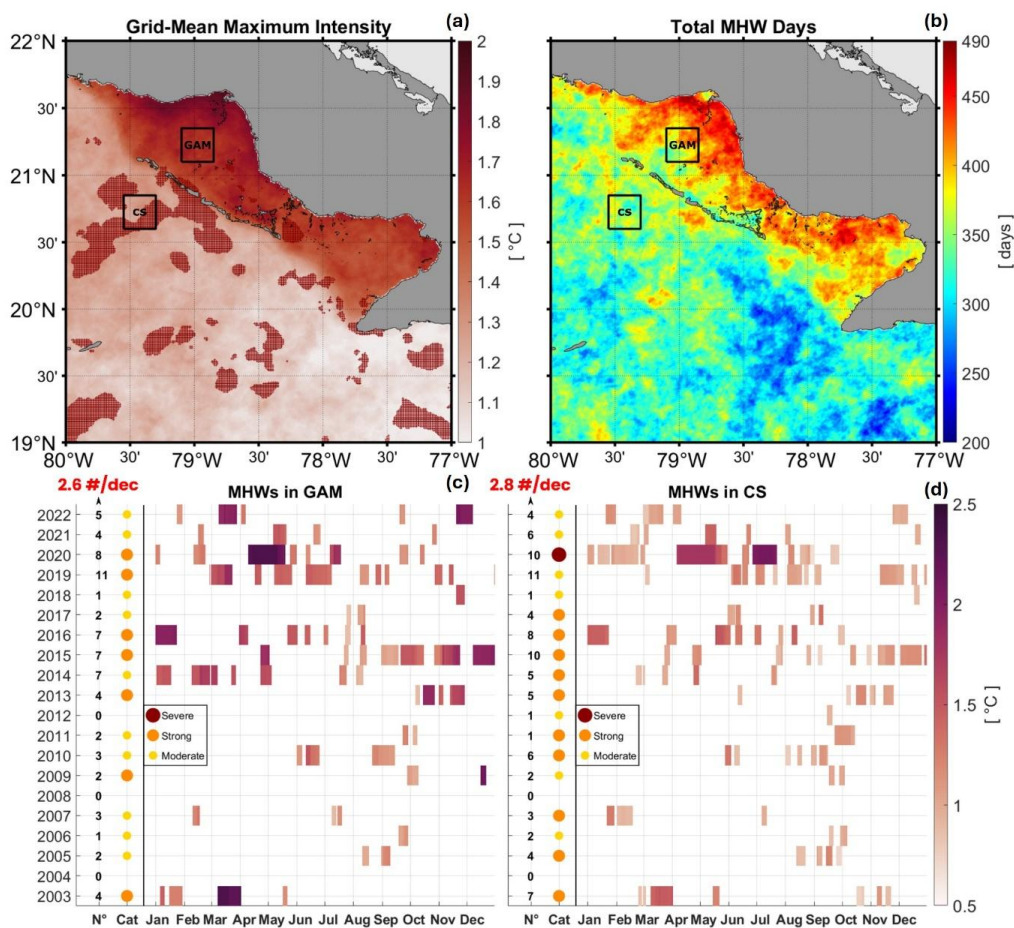
721

722

**Figure 7.** (a,c) Monthly SST anomalies (°C) for the Gulf of Ana María (GAM) and the Caribbean Sea (CS), respectively, 2003–2022. Thin horizontal black lines indicate  $\pm 1$  standard deviation over the full period (value shown in each panel). (b,d) Yearly seasonal means for summer (July–August–September; red squares) and winter (January–February–March; blue squares) in GAM and CS, respectively. Black lines show linear trends of the annual means. Coloured lines show piecewise linear fits to the seasonal means prior to (2003–2011) and after (2012–2022) the 2011 transition. All series represent area averages over the GAM and CS boxes shown in Figures 1a and 1b.



723



724

725

726

727

728

729

730

731

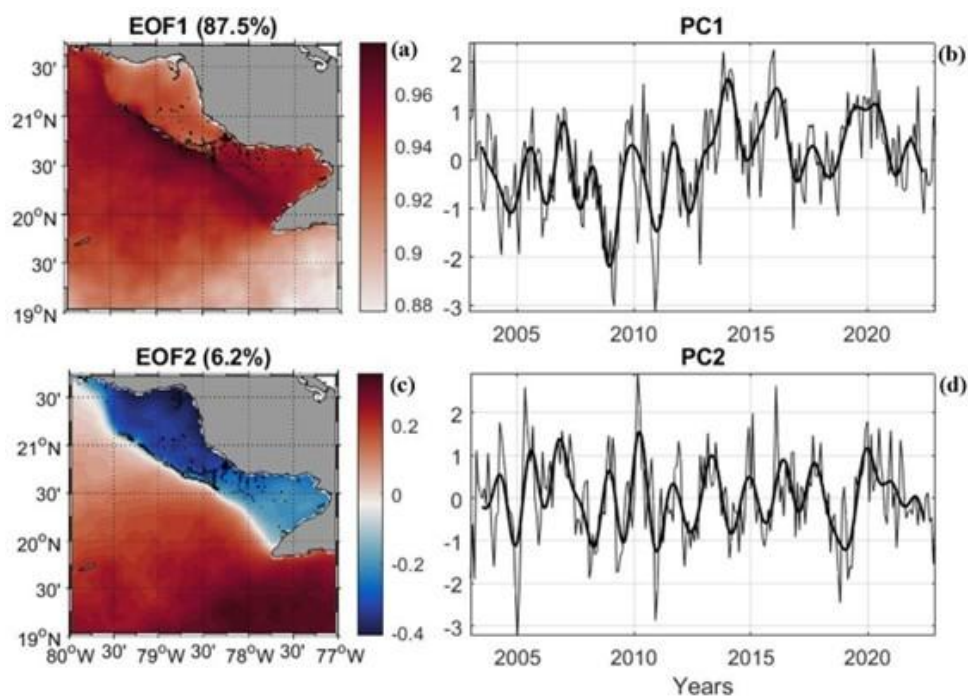
732

733

**Figure 8.** Marine heatwave (MHW) characteristics between 2003–2022. (a) Mean of event-wise maximum intensity (°C) at each grid point. Grid cells that experienced Severe category events at least once are shaded (reddish shading). (b) Total MHW days per grid point accumulated from 2003 to 2022. Black boxes mark the GAM and CS sub-regions. (c–d) Event calendars for GAM and CS, respectively: coloured rectangles denote individual events by month, with darker shading indicating increased intensity (°C). Left-hand columns indicate, for each year, the number of events (N°) and the maximum category reached (circle colour: Moderate/Strong/Severe). At the top left of c-d, the trend in event frequency is shown as the number of events per decade (#/dec).



734



735

736

737

738

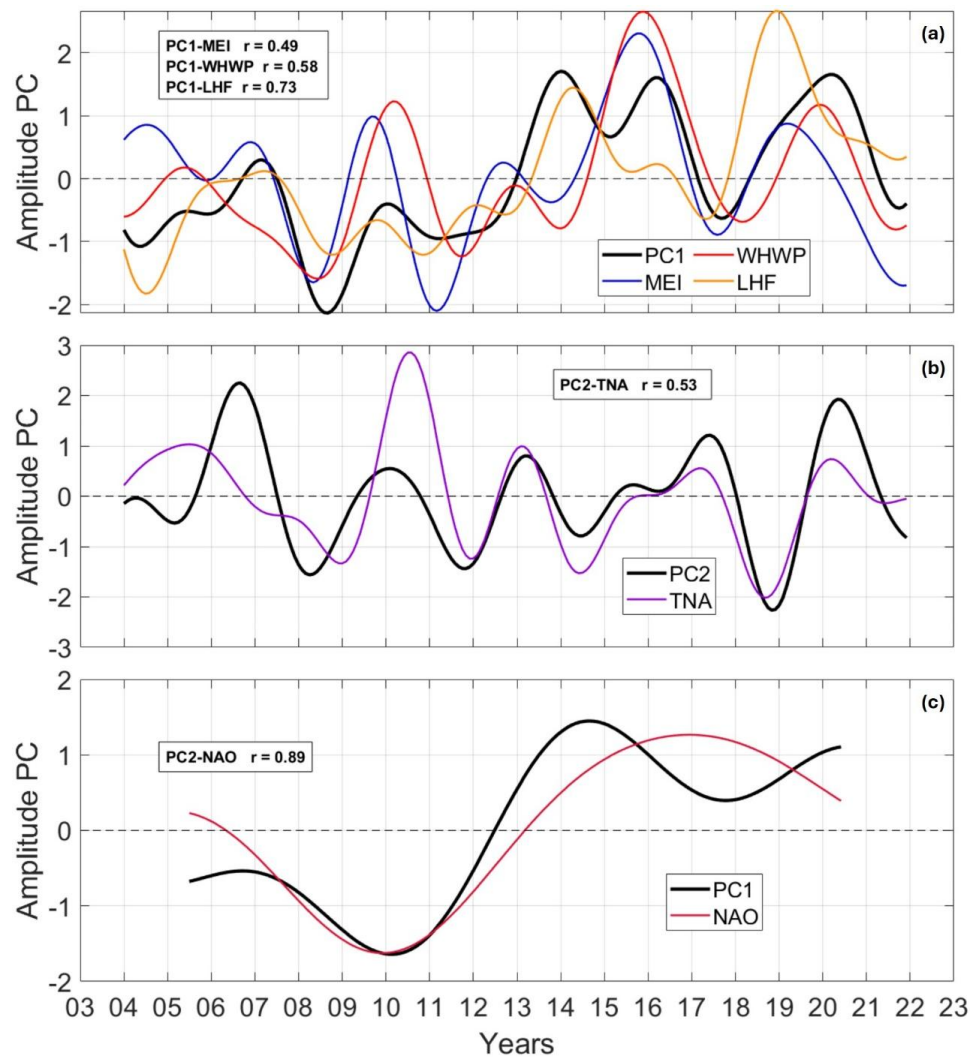
739

740

**Figure 9.** EOF analysis of monthly SST anomalies for 2003–2022. Left: spatial patterns of EOF1 (87.5 %) and EOF2 (6.2 %). Right: Corresponding principal components (PC1, PC2); thick black curve represents a two-year low-pass filter to emphasize interannual variability. (PC signs are arbitrary and chosen so that positive PCs correspond to warm anomalies in EOF1).



741



742

743

744

745

746

747

748

749

**Figure 10.** Co-variability of SST principal components (PCs) with climate drivers. (a) Interannual band: 2-year running-mean low-pass of PC1 (black) plotted with MEI.v2 (blue), Western Hemisphere Warm Pool (WHWP) (red), and domain-mean latent heat flux (LHF) from ERA5 (orange). (b) Interannual band: PC2 (black) with Tropical North Atlantic (TNA) (magenta). (c) Low-frequency band: 5-year running-mean low-pass of PC1 (black) with North Atlantic Oscillation (NAO) (red). Numbers in text boxes denote zero-lag Pearson correlations ( $r$ ) computed on the filtered monthly series. Significance is evaluated using effective degrees of freedom (Section 2.5). Series are standardized.